remote sensing

MDPI

Article

Impacts of Marine Heatwave Events on Three Distinct Upwelling Systems and Their Implications for Marine Ecosystems in the Northwestern South China Sea

Sihai Liu [1,2], Qibin Lao [1,2], Xin Zhou [1,2], Guangzhe Jin [1,3,4], Chunqing Chen [1,2] and Fajin Chen [1,2,3,4,*]

[1] College of Ocean and Meteorology, Guangdong Ocean University, Zhanjiang 524088, China; liusihai@stu.gdou.edu.cn (S.L.); qblao@stu.gdou.edu.cn (Q.L.); xinzhou@stu.edu.cn (X.Z.); jingz@gdou.edu.cn (G.J.); 1112111002@stu.gdou.edu.cn (C.C.)
[2] School of Chemistry and Environment, Guangdong Ocean University, Zhanjiang 524088, China
[3] Key Laboratory for Coastal Ocean Variation and Disaster Prediction, Guangdong Ocean University, Zhanjiang 524088, China
[4] Key Laboratory of Climate, Resources and Environment in Continental Shelf Sea and Deep Sea of Department of Education of Guangdong Province, Guangdong Ocean University, Zhanjiang 524088, China
* Correspondence: fjchen@gdou.edu.cn

Abstract: Under global warming, the frequency and intensity of marine heatwaves are increasing. However, the inhibition of atmospheric-forcing marine heatwaves (AMHW) on upwelling and their impacts on marine ecosystems remain poorly understood. To address this issue, the satellite sea surface temperature and reanalysis data during 1998–2021 were analyzed in three distinct upwelling systems, in the northwestern South China Sea. The results showed that the coastal tide-induced upwelling in the west (W) of Hainan Island is primarily suppressed by enhanced stratification during the AMHW events, since the coastal tide-induced upwelling is insensitive to wind weakening. Contrarily, the wind-driven upwelling in the east (E) and northeast (NE) of Hainan Island are jointly regulated by wind and stratification during the AMHW. Specifically, the AMHW events have a stronger inhibitory effect on the upwelling and phytoplankton growth in the NE than that in the E. The causes could be the following: (1) the background upwelling in the NE region is stronger than in the E; thus, the NE region has a higher susceptibility to the wind weakening; (2) the wind-driven upwelling begins to be suppressed by AMHW when the high-pressure system is aligned with the coastline of the upwelling. In the NE region, the location of the high-pressure center during the occurrence of AMHW is positioned in closer proximity to the upwelling area. Moreover, the inhibitory effect of wind weakening and stratification enhancing on upwelling changes with the development of the AMHW. Before and during the mature phase of AMHW, stratification and wind jointly inhibit upwelling and phytoplankton growth, while a shift to stratification-dominated (>85%) occurs during the decline phase. This study suggests that MHW has a great impact on the upwelling ecosystem, especially the wind-driven upwelling, which should be given high attention under global warming (with increasing MHW events in the future).

Keywords: AMHW; upwelling; wind; stratification; Hainan Island

Citation: Liu, S.; Lao, Q.; Zhou, X.; Jin, G.; Chen, C.; Chen, F. Impacts of Marine Heatwave Events on Three Distinct Upwelling Systems and Their Implications for Marine Ecosystems in the Northwestern South China Sea. *Remote Sens.* **2024**, *16*, 131. https://doi.org/10.3390/rs16010131

Academic Editor: Zhe-Wen Zheng

Received: 14 November 2023
Revised: 21 December 2023
Accepted: 26 December 2023
Published: 28 December 2023

1. Introduction

Upwelling in the ocean is characterized by the ascending motion of seawater, exhibiting velocities typically between approximately 10^{-6} and 10^{-4} m per second [1]. Coastal upwelling is an important component of coastal ocean circulation and is critical for material transport [2,3]. Coastal upwelling contributes over 10% of the global ocean's new productivity [4] and nearly 20% of global fishing yields [5], despite its coverage area accounting for only 1% of global ocean surface. Moreover, upwelling can bring deeper eutrophic water into the upper layer, which can trigger the growth of phytoplankton, thereby changing a series of biogeochemistry processes, such as carbon and nitrogen cycles [6]. Therefore, upwelling plays an extremely important role in global marine ecology and climate change [7,8].

Marine heatwaves (MHW) are sustained anomalies in sea surface temperature (SST)that exceed the climatological threshold and have severe impacts on marine ecosystems [9–11]. Substantial subtropical MHW are predominantly triggered by persistent atmospheric high-pressure systems, which are linked to amplified solar radiation and unusually weak wind speeds [12]. The close association among underlying atmospheric processes, MHW, and upwelling accentuates the crucial need to study their impacts on upwelling and ecosystem dynamics, particularly in the context of intensifying MHW. Some previous studies have shown the role of upwelling in mitigating MHW, such as the fewer MHW days near major eastern boundary upwelling systems than in open ocean regions [13,14]. However, the impact of MHW on upwelling has been largely ignored [15–17]. In nutrient-limited tropical and subtropical regions, the enhanced stratification resulting from marine heatwaves ultimately leads to a reduction in surface availability of nutrients and Chl-*a* concentration [18]. To date, the understanding of the extent and mechanism of the impact of MHW on different distinct upwellings remains unclear.

The South China Sea (SCS) is a large semi-enclosed marginal sea basin situated at the northwestern Pacific Ocean (99–125°E, 0–25°N). During the period 1982–2019, MHW events in the SCS became more frequent, intense, widespread, and severe. According to a diagnosis of synoptic-scale heat budgets, the extreme warming in the SCS is primarily associated with near-surface anticyclonic anomalies, which often accompany the westward extension of the Western Pacific Subtropical High [19,20]. Regarding the relationship between MHW and upwelling in the SCS, previous studies have primarily emphasized the decrease in Chl-*a* concentrations during MHW periods in the Western SCS, attributed to the weakening of upwelling [21], with limited research delving into the detailed process of MHW inhibiting upwelling.

The SCS experiences upwelling-favorable southern winds during summer due to the influence of the East Asian monsoon [22]. Hainan Island is situated on the northwestern continental shelf of the SCS; there are three distinct upwellings around Hainan Island (Figure 1). The upwellings in the eastern (E) and northeast (NE) regions of Hainan Island are driven, respectively, by the southwest and southeast monsoons [23–25]. Furthermore, Ekman pumping induced by wind stress curl is regarded as another crucial factor in generating upwelling in E and NE regions [26], and even as the primary cause of interannual variability in the upwelling of the E regions [27,28]. Variations in coastal topography significantly contribute to the formation of upwelling centers distributed in the E and NE regions [1]. In addition to wind, topography, ocean currents, eddies, and tides have also been reported as significant factors influencing the upwelling in the northeastern region [23,29,30]. On the contrary, the upwelling on the west (W) of Hainan Island is mainly induced by stratification and tides [24,31,32]. Firstly, the W region is generated by two factors. Firstly, stratification is formed in the upper layer of the middle area of the Beibu Gulf due to the increase in heat flux during spring and summer. The water retained from the previous winter forms a cold water mass below the thermocline [31,32]. Secondly, a tidal front is formed between the mixing zone and the stratification zone in the middle of the Beibu Gulf due to strong tidal mixing along the coastal area on the west side of Hainan Island. The difference in pressure gradients on either side of the tidal front eventually forms the W region [33–35]. Therefore, the causes of the upwellings along the coast of Hainan Island are significantly different, with the eastern and northeastern upwelling mainly related to the monsoon and the W region mainly related to the summer stratification and the tidal front in the Beibu Gulf. Thus, the northwestern SCS is an ideal area to carry out a systematic study about the impact of heatwaves on upwelling.

Here, we integrate satellite and reanalysis daily data from 1998 to 2021 to investigate the factors influencing the changes in upwelling associated with different causal mechanisms during the AMHW events, considering both the temporal and spatial distributions of synthetic event sequences. Furthermore, we quantify their contributions to the variations in upwelling during different phases of the AMHW, aiming to elucidate the impact of the AMHW on upwelling driven by various causal mechanisms.

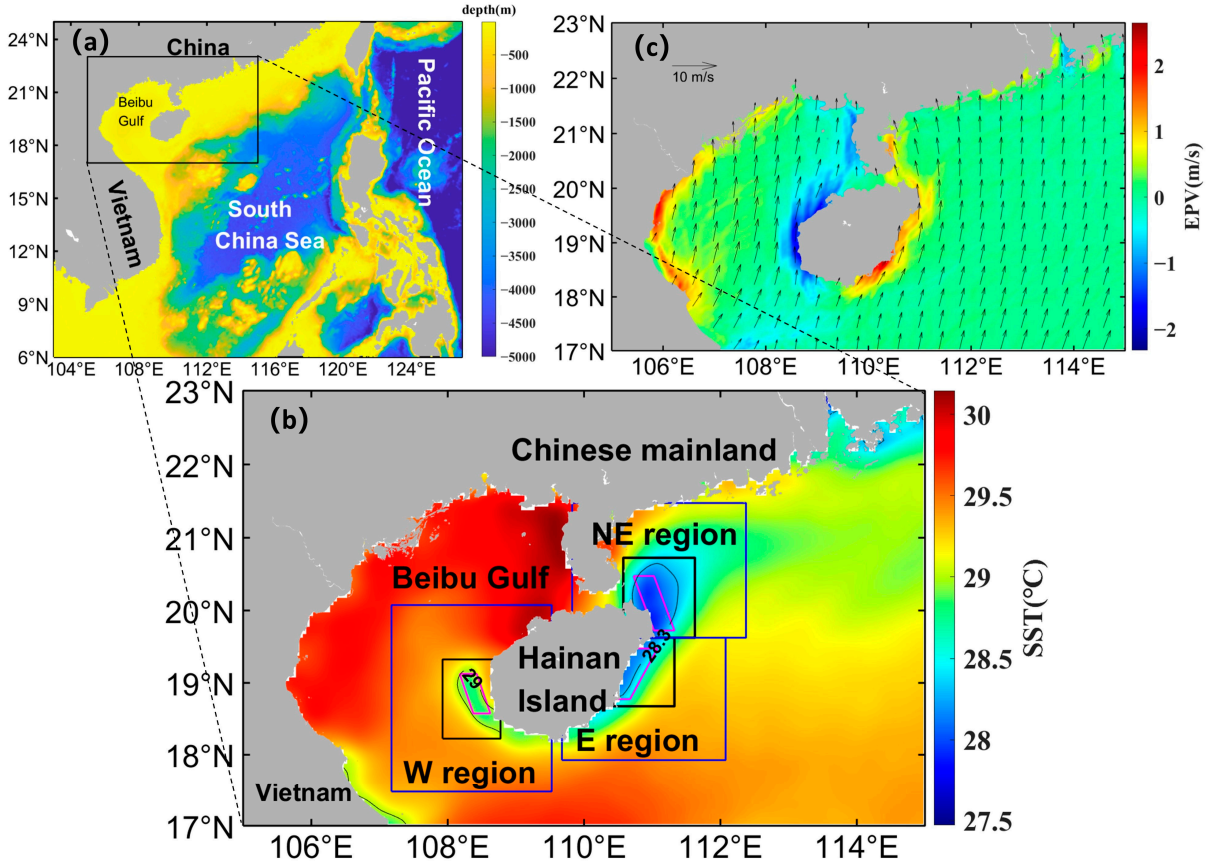

Figure 1. Location and Topography of the Study Area (**a**), Spatial Distribution of SummerAveraged SST (**b**), Mean Wind Speed and Ekman Pumping Velocity (**c**) over Multiple Years (1982–2021). In (**b**), the pink parallelograms represent the core regions of upwelling, the black rectangles represent the areas potentially affected by upwelling, and the blue rectangles represent the non-upwelling areas (with the exceptions of the black rectangles). NE region represents 19.6–21.5°N, 109.8–112.4°E; E region represents 17.9–19.6°N, 109.7–112.1°E; and W region represents 17.5–20.1°N, 107.2–109.5°E. In (**c**), positive velocity means upwelling.

2. Data and Methods

2.1. Data Sources

The intensity of MHW [36] can be derived from SST obtained from the OSTIA (an operation, real-time, high-resolution, global SST analysis system, https://data.marine.copernicus.eu/product/SST_GLO_SST_L4_REP_OBSERVATIONS_010_011; accessed on 1 July 2023) daily SST images with a 0.05° × 0.05° resolution [37]. ERA5 is a global climate atmospheric reanalysis produced by the European Centre for Medium-Range Weather Forecasts [38], which is the fifth generation in the series (https://cds.climate.copernicus.eu/cdsapp#!/dataset/reanalysis-era5-single-levels-monthly-means; accessed on 1 July 2023). This reanalysis provides hourly estimates of various atmospheric, land, and oceanic variables from 1979 to 2023. The present study utilizes several key variables, including daily mean net surface solar radiation, 10 m wind speeds as well as mean sea level pressure. The spatial resolution of the dataset is 0.25 degrees. The Chl-*a* daily L4 dataset, covering the time period from 1997 to 2022, was obtained from the Global Ocean Color (Copernicus GlobColour) database (https://data.marine.copernicus.eu/product/OCEANCOLOUR_GLO_BGC_L4_MY_009_104; accessed on 1 July 2023) with a spatial resolution of 4 × 4 km.

2.2. Method

In the context of oceanographic dynamics, Ekman transport is modulated by the interactive forces of wind stress and the Coriolis effect. This interaction fosters a convergence

and divergence in marine waters, subsequently exerting an impact on the velocity of Ekman pumping (referred to as *EPV*) [39].

$$EPV = curl\left(\frac{\tau}{\rho f}\right) \tag{1}$$

where ρ and f represent the density of sea water and the Coriolis coefficient, respectively. The coefficient can be quantified as $2\omega \sin \theta$, where ω symbolizes the Earth's angular velocity of rotation and θ embodies the geographical latitude. $\vec{T}$ is wind stress, which was calculated as follows:

$$\vec{\tau} = \rho_a \cdot C_d \cdot \left|\vec{U}\right| \cdot \vec{U} \tag{2}$$

where ρ_a is the air density, $\vec{U}$ is the wind vector at 10 m above sea level, and C_d is the drag coefficient, which was calculated as follows [40]:

$$C_d = \begin{cases} \left(0.29 + \frac{3.1}{|\vec{U}|} + \frac{7.2}{|\vec{U}|^2}\right) \times 10^{-3}, 3 \le |\vec{U}| \le 6 \text{ m/s} \\ (0.60 + 0.071|\vec{U}|) \times 10^{-3}, 6 \le |\vec{U}| \le 26 \text{ m/s} \end{cases} \tag{3}$$

The wind curl was calculated using the wind stress:

$$curl\ \vec{\tau} = \frac{\partial \tau_x}{\partial y} + \frac{\partial \tau_y}{\partial x} \tag{4}$$

In line with Hobday et al. [36], several tools have been developed to automatically detect and provide statistical descriptions of MHW events [41]. In this study, we utilized the MATLAB implementation developed by Zhao and Martin [42], which is publicly available at https://github.com/ZijieZhaoMMHW/m_mhw1.0 (accessed on 1 March 2023). Detail parameters for MHW detection followed Matlab tool defaults: spatial climatology and threshold were calculated with a 5-day sliding window; MHW events were identified using a 90th percentile threshold; spatial climatology and threshold smoothing employed a 31-day moving mean window; a minimum 5-day duration was required for MHW event recognition, and a maximum 2-day gap was permitted for joining successive MHW events.

$$T_m(j) = \sum_{y=y_s}^{y_e} \sum_{d=j-5}^{j+5} \frac{T(y,d)}{11(y_e - y_s + 1)} \tag{5}$$

$$i_{mean} = \overline{T(t) - T_m(j)} \tag{6}$$

The climatological SST mean (T_m) used in this study was calculated from 1 January 1982 to 31 December 2011, and the daily SST on day d of year y is represented by T.

In order to investigate AMHW across the entire region rather than focusing on localized small grid points [43], we selected mean SSTas the indicator for AMHW events. This approach effectively eliminates small-scale ocean processes and enhances the discernibility of larger-scale atmospheric influences on AMHW events. Additionally, the weakening upwelling can also lead to MHW [44]. Thus, we excluded the upwelling areas (as shown in black rectangles in Figure 1b) and retained only the SST from non-upwelling regions surrounding them as indicators of AMHW events to avoid potential causal inversion resulting from feedback processes. As the average duration of heatwaves in this study was 11 days, short-term surface heating in the upwelling regions would not significantly alter the temperature at the bottom of the seawater [45]. Therefore, the difference between the density derived from the SST and climatological mean salinity in the upwelling region and the climatological density was utilized as an indicator of seawater stratification during the AMHW event.

The extent of the upwelling is defined by the climatological mean SST, where the general range of the upwelling is initially determined by isotherms (29 °C and 28.3 °C

isotherm for the west and east of Hainan Island, respectively). Subsequently, considering the shape of the coastline and the isotherms, core regions representing the characteristics of upwelling in different regions are further selected as the focus area of the study (as shown in pink parallelograms in Figure 1b). Due to the larger extent of upwelling off the eastern coast of Hainan Island, it is further divided into the eastern and northeastern parts, respectively. To decouple the MHW events from upwelling events, the average temperatures of the non-upwelling areas surrounding the upwelling areas are selected as criteria for identifying AMHW occurrences (Figure 1b), because atmospheric high-pressure systems typically influence the sea areas near the high-pressure centers. Accordingly, from 1998 to 2021, a total of 28, 30, and 31 independent AMHW events were identified in the E, NE, and the upwelling in the WH (W) regions, respectively. Events in different regions occasionally occur on the same date.

To better illustrate the inhibitory effect of AMHW on different upwelling regions, Figure 2 presents the spatially synthesized distribution of the periods before, during, and the difference between the periods for each region. This is based on the average duration of AMHW events and the changes of variables over time, as detailed in Figures 3 and 4. Pre-AMHW refers to the days in the E and NE regions that were influenced by AMHW but did not exhibit significant warming, ranging from −10 to −6 days (with the day of heatwave occurrence designated as 0). The time period affected by AMHW in the E and NE is defined as during AMHW, ranging from −5 to +11 days. Compared to the E and NE regions, the wind stress and Chl-*a* in the W region reach their peak values in a shorter time before the maturation of AMHW (Figure 4a,c). Therefore, pre-AMHW in the W region is defined as −5 to −1 days, and the AMHW period is defined as 0 to +11 days.

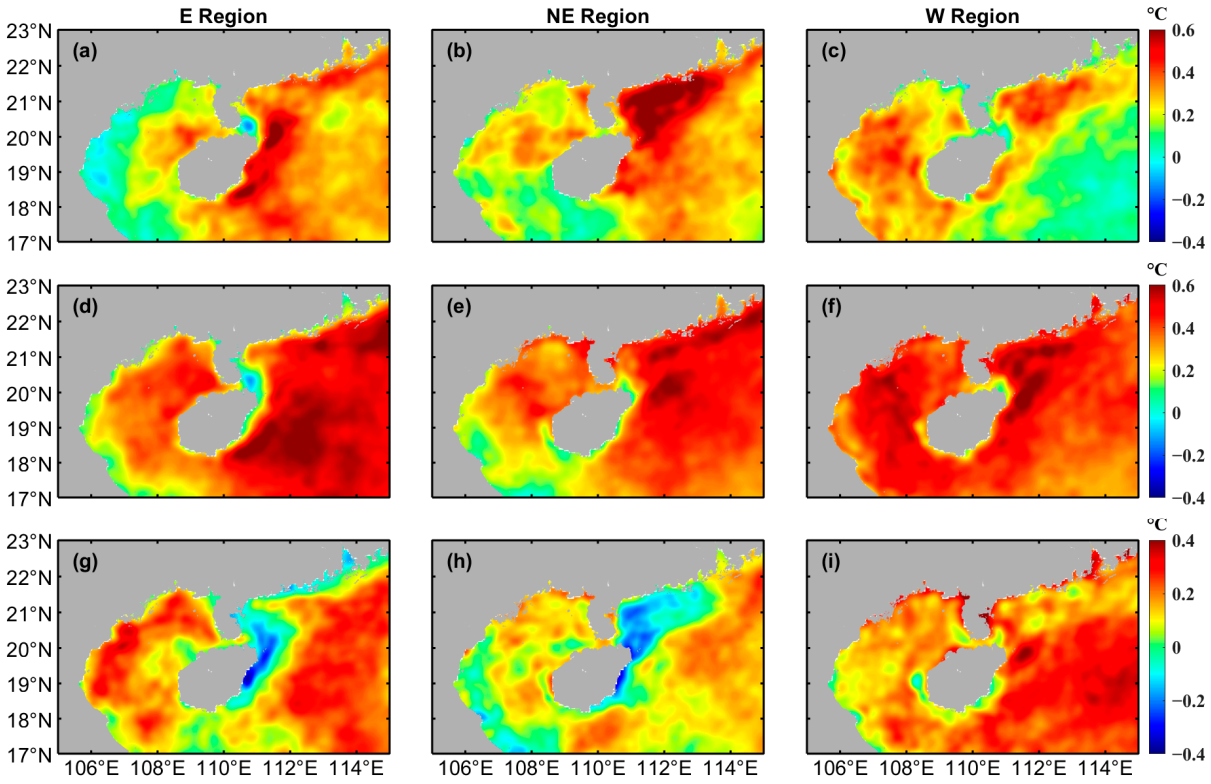

Figure 2. Spatial Distributions of SST Anomalies in Three Upwelling Regions During Different Phases of AMHW. Panels (**a**–**c**) show the difference (Delta) in SST anomalies, panels (**d**–**f**) illustrate SST anomalies during AMHW, and panels (**g**–**i**) depict SST anomalies in the Pre-AMHW phase. Each column corresponds to a specific region, with (**a**,**d**,**g**) for the E Region, panels (**b**,**e**,**h**) for the NE Region, panels (**c**,**f**,**i**) for the W Region.

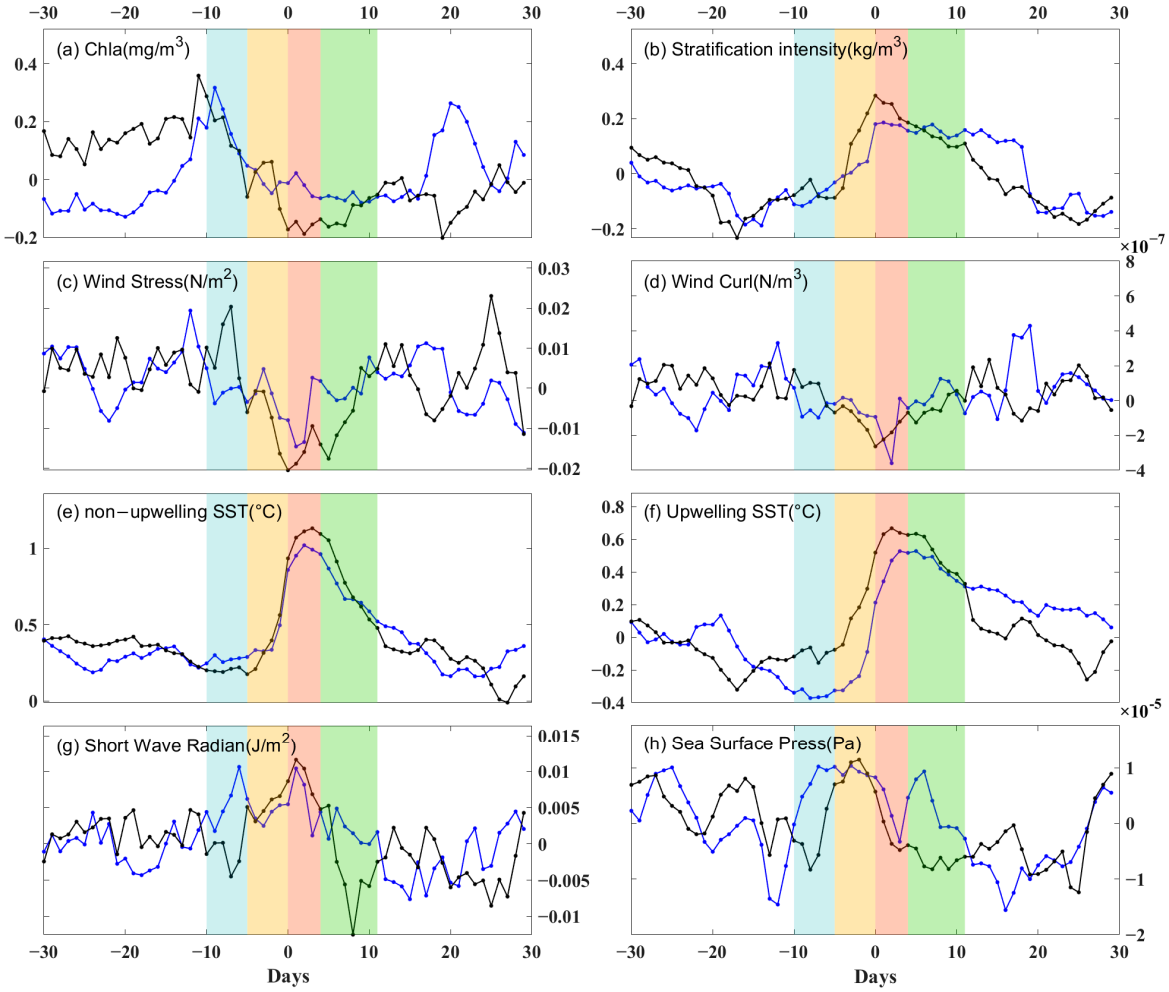

Figure 3. Variations in Relevant Indicators of Region E (blue curve) and Region NE (black curve) during the 30 days before and after the occurrence of AMHW (synthetic average of all summer heatwaves from 1998 to 2021). Day 0 represents the first day of heatwave occurrence. The blue region represents the pre-AMHW phase, while the orange, red, and green regions represent the development phase, mature phase, and decline phase of AMHW, respectively.

In addition, Pearson correlation coefficients were employed to analyze the relationships, and the xcorr function in MATLAB 2021a was used to compute the normalized cross-correlation coefficients between two vectors at all possible lags. To investigate the patterns of short-term AMHW events, daily anomalies of all data from the summer seasons of 1998–2021 were utilized to remove long-term trends and seasonal variations.

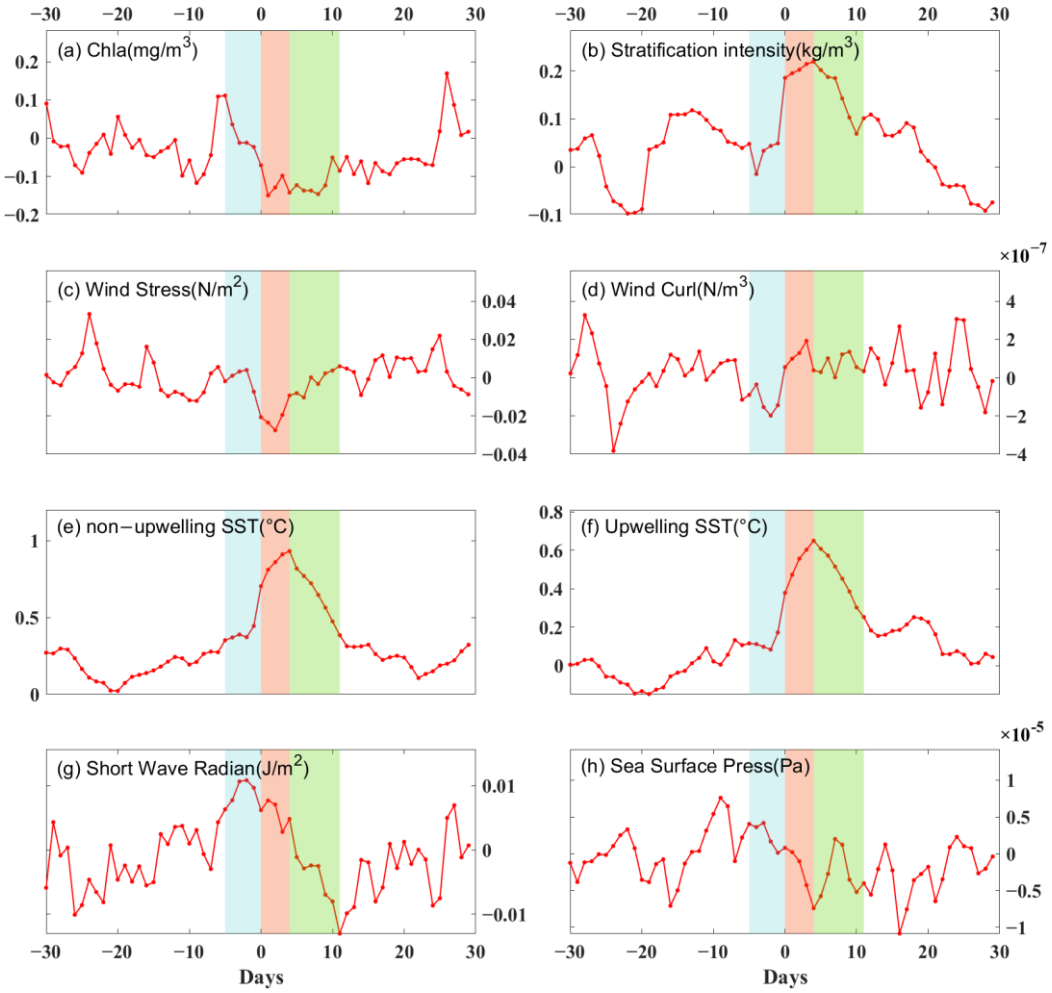

Figure 4. Variations in Relevant Indicators of Region W during the 30 days before and after the occurrence of AMHW (synthetic average of all summer heatwaves from 1998 to 2021). Day 0 represents the first day of heatwave occurrence. The blue region represents the pre-AMHW phase, while the red and green regions represent the mature phase and decline phase of AMHW, respectively.

3. Results

In the summer, influenced by the southwest monsoon (Figure 1c), wind-induced upwelling occurs along the eastern coast of Hainan Island, where the SST in the upwelling area is generally 1–2 °C lower than the surrounding waters. Similarly, upwelling is observed in the W region, but it is generally weaker than the upwelling along the eastern coast of Hainan Island, with a SST about 0.5–1 °C lower than the surrounding waters. During the pre-AMHW, the SST climatic anomalies in E and NE regions are negative, indicating a significant enhancement of upwelling (*t*-test, $p < 0.001$, Figure 2g–i). In contrast, there is no significant enhancement of upwelling in the W region before the occurrence of AMHW. During the AMHW events, the SST anomalies in the upwelling regions rapidly increased and then slowly decreased (Figure 3e,f and Figure 4e,f). The spatial distribution of the difference between AMHW and pre-AMHW periods varies significantly among the three regions (Figure 2a–c). The SST differences between the AMHW period and the pre-AMHW period exhibit notable spatial variations across different upwelling regions. For instance, the SST differences in the E and NE during the AMHW period are predominantly localized with local extreme values in their respective areas, while the difference in the W during the AMHW period shows maximum values in the northwestern part of the study area. This indicates the spatial heterogeneity of AMHW rather than synchronous warming in the surrounding waters (Figure 2a–c).

From a temporal perspective, the period 5 days prior to the occurrence of a heatwave is considered as the development phase of the associated AMHW. During this phase, SST begins to show an increasing trend. From the day of heatwave occurrence and the following 4 days, the AMHW enters the mature phase, during which the intensity of the AMHW rapidly increases and reaches its peak (Figure 3e). Subsequently, the AMHW enters the decline phase, which is defined as the duration of AMHW events (11 days) minus the duration of the mature phase (4 days). Due to the rapid development of heatwaves in the W region, the wind speed starts to weaken only one or two days before the maturity of the heatwave, and thus, the W region does not have a defined development phase. SST continues to decrease for 1 to 2 weeks after the end of the heatwave until it reaches a steady value similar to that before the occurrence of the heatwave. The climatic anomaly of SST in the upwelling regions decreases to negative values before the occurrence of AMHW (with a less noticeable decrease in the W region, approximately around 0.1 °C). However, with the development of the heatwave, the SST increases to very high positive values (Figures 3f and 4f). Due to the consistently positive climatological SST anomalies in the non-upwelling area, the negative anomalies in the E and NE region are evidently caused by the intensification of upwelling (Figure 3e,f). This indicates that before the development phase of an AMHW, external conditions positively promote wind-driven upwelling, but as the heatwave develops, the favorable external conditions for upwelling gradually diminish. The upwelling regions exhibit weaker warming and slower cooling rates compared to the non-upwelling regions, reflecting the inhibitory effect of upwelling on the AMHW and the stability of SST in the upwelling regions. During the maturation of AMHW, there are often several consecutive days of high-pressure weather, characterized by weak winds, few clouds, and strong shortwave radiation (Figure 3c–e). In the NE and E regions, wind stress is positively correlated with wind stress curl, while in the W region, wind stress is negatively correlated with wind stress curl (Figure 3c,d and Figure 4c,d). Therefore, during the period of an AMHW, the Ekman pumping effect may have an opposite impact on upwelling.

Notably, during an AMHW event and a subsequent period (−5 to +30), the concentrations of Chl-*a* in the three upwelling regions generally exhibit a High–Low–High trend. The low values are generally negative, and the duration encompasses the entire AMHW phase (Figures 3a and 4a). During the pre-AMHW period, Chl-*a* exhibits predominantly positive anomalies, indicating the strengthening of upwelling. Following the decline of the AMHW, it takes approximately two weeks for Chl-*a* to gradually return to the climatological mean, highlighting the sustained impact of the brief AMHW event on upwelling.

To further investigate the inhibitory effects of AMHW on upwelling intensity and the ecosystem, the correlation plots of various variables during the 11 days before and after the occurrence of AMHW were conducted in this study (Figure 5). As heatwaves are short-term events and may occur multiple times within a period, we focused on discussing the data in the immediate vicinity of the heatwave occurrence as its influence. The concentrations of Chl-*a* in all three regions showed a strong relationship with stratification intensity ($|r| > 0.7$, $p < 0.05$), indicating the significant impact of stratification on upwelling during heatwave events. In the NE region, there is a close correlation among Chl-*a*, stratification intensity, and wind stress, with correlation coefficients exceeding 0.7 ($p < 0.05$), reflecting the strongest influence of heatwaves on the NE upwelling region. The cross-correlation coefficient between wind stress and Chl-*a* in the E region has a time lag; as the time lag increased to the fourth day, the cross-correlation coefficient between them increased from near 0 to a peak value of 0.6 (Figure 6). Finally, to quantify the effects of wind stress reduction and stratification intensification (the two main processes of AMHW) on the concentrations of Chl-*a*, the delayed Chl-*a* concentration was subjected to correlation analyses with both wind stress and stratification intensity. It was found that Chl-*a* showed a clear linear relationship with wind stress and stratification intensity during the AMHW period. In the E region, the two sets of linear relationships have R^2 values of 0.47 and 0.52,

respectively, in the NE region; R^2 values are 0.51 and 0.66, and in the W region, R^2 values are 0.37 and 0.56 (all p-values < 0.05, Figure 7).

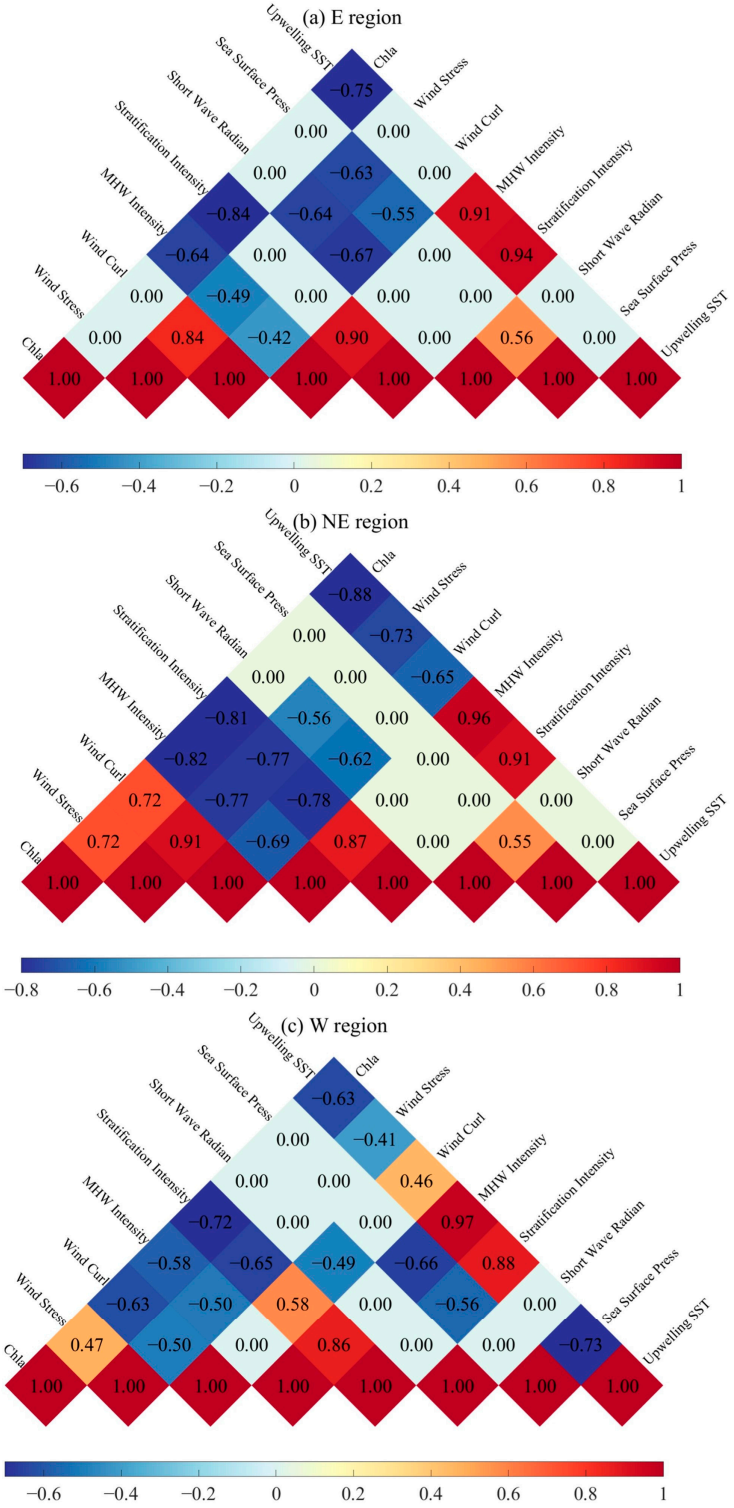

Figure 5. Correlation Analysis of Composite Heatwave Sequences for the 11 Days Before and After the First Day of AMHW Occurrence. Panels (**a**–**c**) represent Regions E, NE, and W, respectively. The composite heatwave sequences are derived from the composite average of all summer heatwaves from 1998 to 2021.

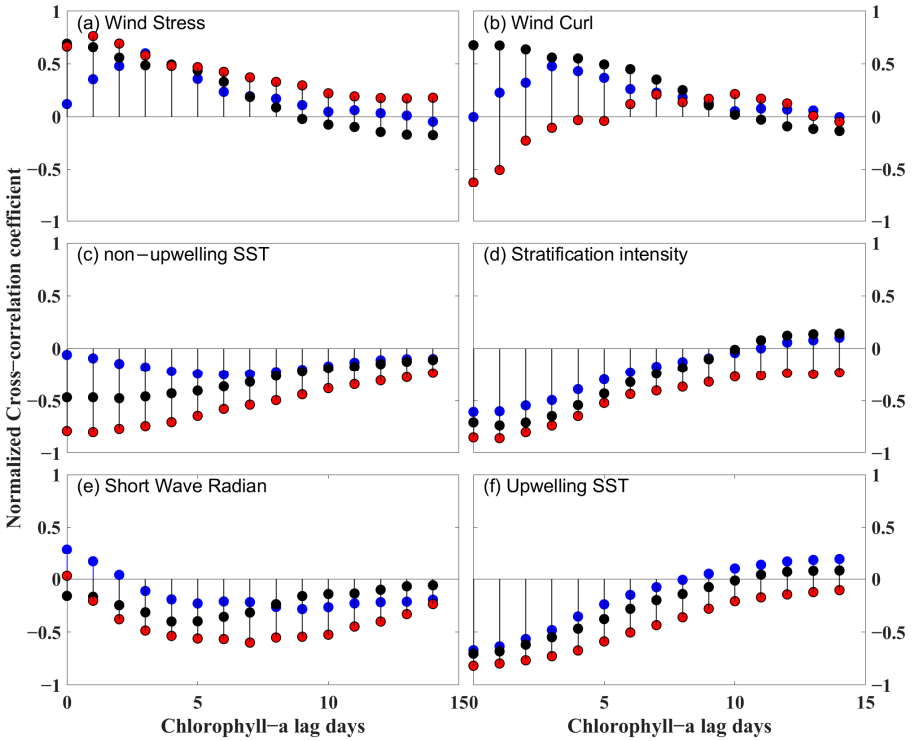

Figure 6. Lagged Correlation Analysis of Various Indicators with Chl-*a* in Regions E (blue), NE (black), and W (red). The time series indicators are derived from the synthetic heatwave sequence, with a consistent length of 23 days, as described in Figure 5.

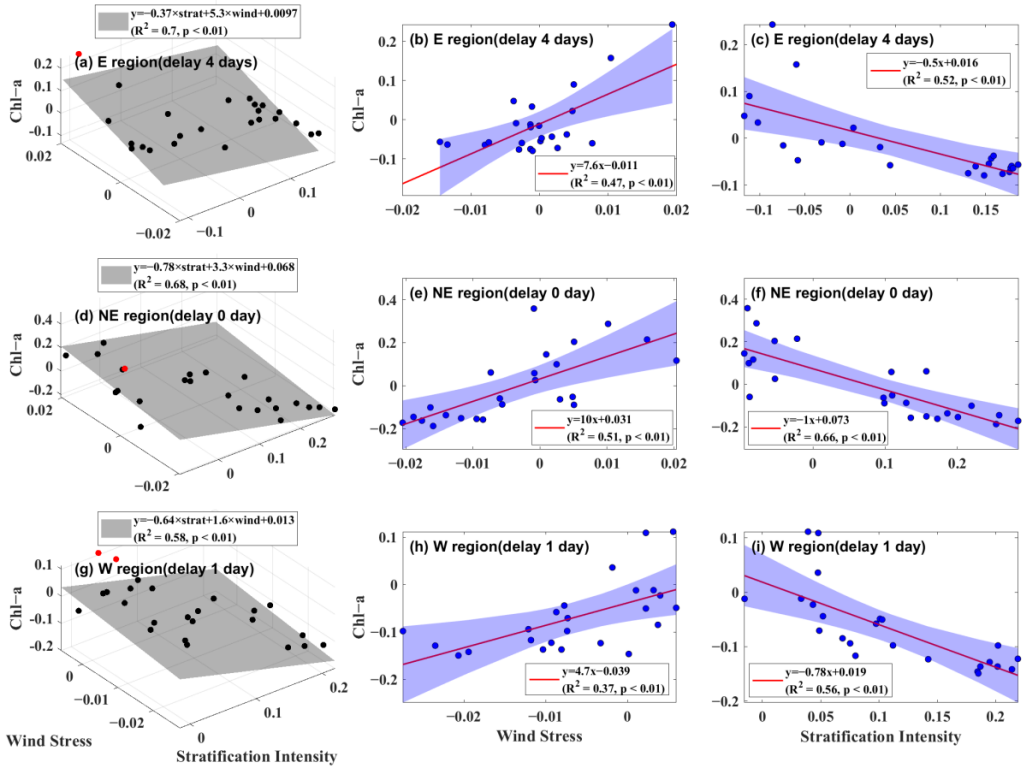

Figure 7. Detailed Linear Regression Analysis of Chl-*a* with Wind Stress and Stratification Intensity in Regions E, NE, and W. Panels (**a**,**d**,**g**) display multiple linear regression of Chl-*a* against wind stress and stratification. Panels (**b**,**e**,**h**) illustrate simple linear regression of Chl-*a* against wind stress, while panels (**c**,**f**,**i**) present simple linear regression of Chl-*a* against stratification. The red dots in panels (**a**,**d**,**g**) represent data points outside the 95% confidence interval.

4. Discussion

4.1. Wind Weakening and Stratification Enhancing during AMHW Events

The occurrence of AMHW can be mainly attributed to strong weather patterns, such as persistent high-pressure systems and atmospheric blocking, as well as reduced cloud cover and precipitation [12,46–48]. The Western North Pacific Subtropical High is the dominant circulation system in the summer climate of the Western Pacific [49], and the anomalies of the Western North Pacific Subtropical High can cause abnormal monsoon patterns and various extreme weather events in the Western Pacific, including the northwestern SCS [50–53]. In this study, under the influence of the Western North Pacific Subtropical High, the frequent conditions of clear sky, low cloud cover, and weak wind lead to a significant increase in surface shortwave radiation [54,55]. This hot and dry weather provides favorable conditions for the occurrence of AMHW.

Since the average duration of a heatwave is approximately 11.1 days, we conducted a correlation analysis of the variables by examining the changes in each variable during the 12 days before and after the maturity of AMHW (referred to as day 0). The results are shown in Figures 5 and 6. The sea-level atmospheric pressure reaches its peak at around −2 to −1 days before the maturation of AMHW. During the pre-AMHW period, the wind stress in the three upwelling regions initially increases to a positive climatic anomaly and then decreases continuously until reaching its lowest value 2–3 days after the peak of sea-level atmospheric pressure (Figures 3 and 4c,d,h). Due to the higher terrain of Hainan Island, the south winds blowing over Hainan Island generate a positive wind stress curl on the eastern side and a negative wind stress curl on the western side (Figure 1c). Both wind stress curls in the NE and E regions positively correlate with the change in wind stress, with correlation coefficients of 0.84 and 0.91, respectively (both $p < 0.05$). In the W region, however, the wind stress curl changes negatively correlated with wind stress, with a correlation coefficient of −0.50 ($p < 0.05$). Furthermore, these findings, however, introduce concerns of collinearity due to the synchronized changes in both factors, thus complicating the isolation of their individual contributions to the weakening of the upwelling. To resolve this, the wind's influence in the subsequent discussion is represented solely by wind stress magnitude. It should be noted, though, that this discussion inherently includes the effects of both Ekman transport and Ekman pumping on upwelling.

In addition, the anticyclonic center (high-pressure center) of low wind speed before the occurrence of the AMHW is mostly located on the eastern side of the corresponding upwelling regions (Figure 8g–i). Although the high-pressure center does not appear in the pre-AMHW period of the NE region, it can be inferred to be on the eastern side of the study area according to the wind rotation (Figure 8g–i). As the heatwave develops, the high-pressure center starts to extend westward, consistent with the variations of the Northwestern Subtropical High [56]. This keeps the upwelling regions in a state of weak winds until the high-pressure center moves away. During the AMHW period, the climatic anomaly of surface net shortwave radiation also shows an increasing and then decreasing trend, reaching its highest value of 0.01 J/m^2 at +1 day (Figures 3g and 4g). This trend is similar to the change in wind stress and lags behind the atmospheric pressure change by 2–3 days. The density difference representing the stratification effect reaches its maximum value of approximately 0.2 kg/m^3 at +3 days (Figures 3b and 4b).

4.2. The Inhibitory Effects of AMHW on Upwelling

The SST difference and temperature point index (TPI) are widely used as indicators for the intensity of coastal upwelling [57–60]. However, due to the inhibitory effect of upwelling on rapid warming and heatwave occurrences [13,14,61], the SST difference and TPI value in the upwelling regions tend to be amplified, resulting in false signals of

enhanced upwelling. Wind stress is considered another important indicator for the intensity of coastal upwelling, such as the Bakun Index. This index utilizes the coastal component of wind stress to estimate nearshore Ekman transport [62,63]. However, the Bakun Index does not represent the variations of oceanic conditions during the wind-driven upwelling events. Moreover, the variation in the oceanic stratification effect becomes significant when SST increases rapidly during AMHW. Therefore, additional indicators are needed to characterize the changes in upwelling during AMHW. Upwelling can transport nutrients from the deeper water to the surface [64]. A short-term variation in Chl-*a* associated with coastal upwelling also shows that phytoplankton growth is approximately 2 days later than upwelling activity [65,66]. Thus, the variation in Chl-*a* resulting from upwelling can effectively reflect the influence of stratification and wind on upwelling.

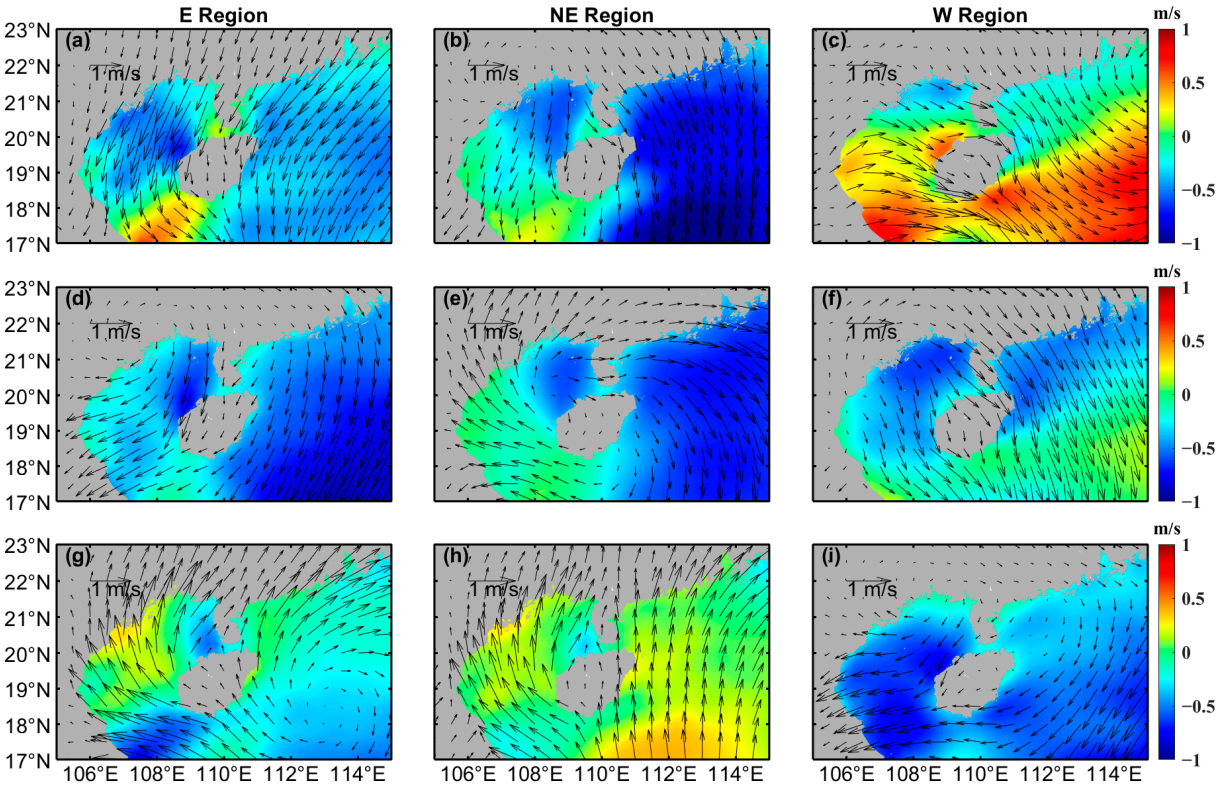

Figure 8. Spatial Distributions of Wind Vector Anomalies and Wind Anomalies in Three Upwelling Regions During Different Phases of AMHW. Panels (**a**–**c**) depict the Delta (During-Pre), panels (**d**–**f**) the AMHW period, and panels (**g**–**i**) the Pre-AMHW phase, each showcasing wind vector anomalies and wind anomalies. Each column corresponds to a specific region, with (**a**,**d**,**g**) for the E Region, panels (**b**,**e**,**h**) for the NE Region, panels (**c**,**f**,**i**) for the W Region.

Due to the different coastlines, the upwelling in the E and NE regions is generated by southwest and southeast winds, respectively [67], whereas the W region experiences a combination of tidal-induced upwelling and wind-induced downwelling [35]. In this study, the three upwelling regions undergo changes with variations in the wind field during AMHW (Figures 8 and 9). Prior to AMHW maturation, the climatological anomalies in wind speed in the E and NE regions are positive; and the climatological anomalies of wind vectors are southeasterly and southerly winds, both conducive to upwelling. Accordingly, the climatological anomalies of Chl-*a* in these two regions significantly increase (Figures 8g and 9f–h). In the mature phase of AMHW events in the E and NE regions, there is a significant change in the wind vector anomalies compared to the pre-AMHW conditions. The anomalies in the NE region shift to northwesterly winds, while the anomalies in the E region shift to northeasterly winds, which are unfavorable for upwelling and result in a significant reduction in Chl-*a* at the corresponding locations (Figure 8a,b and Figure 9a,b).

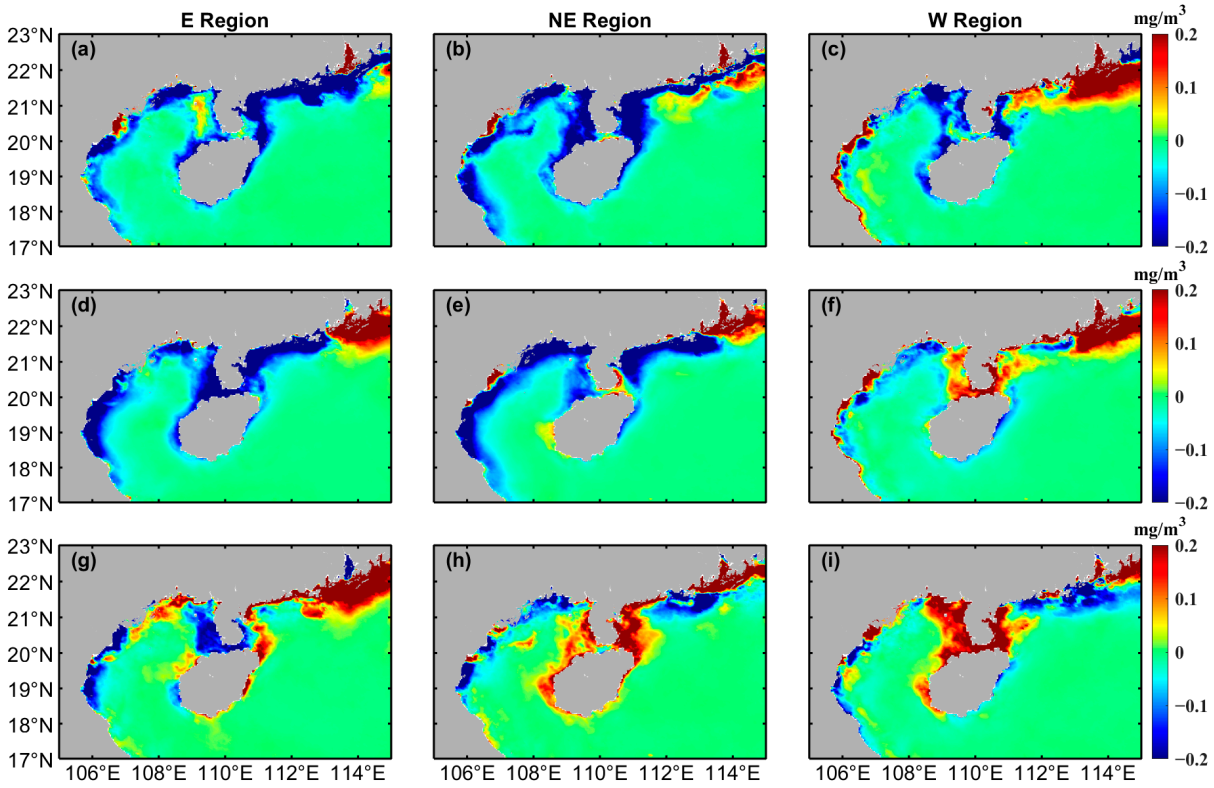

Figure 9. Spatial Distributions of Chl-*a* Anomalies in Three Upwelling Regions During Different Phases of AMHW. Panels (**a**–**c**) depict the Delta (During-Pre), panels (**d**–**f**) the AMHW period, and panels (**g**–**i**) the Pre-AMHW phase, each showcasing Chl-*a*. Each column corresponds to a specific region, with (**a**,**d**,**g**) for the E Region, panels (**b**,**e**,**h**) for the NE Region, panels (**c**,**f**,**i**) for the W Region.

It is worth noting that the weakening of upwelling in the NE region during an AMHW events is more pronounced than in the E region (Figure 3a), and this may be attributed to multiple factors. Firstly, following the weakening of the generating variables, namely wind, the stronger pre-existing upwelling in the NE region compared to the E region (Figure 1b) may render it more susceptible to suppression. Secondly, the NE region exhibits stronger vertical turbulent mixing that aids in the upward transport of water [23], and numerical studies by Bai et al. also revealed that local intense mixing favors the growth of upwelling in the NE region [68]. Therefore, when the wind, which plays a crucial role in promoting mixing, weakens, the weakening of upwelling in the NE region becomes more pronounced. Lastly, the coupling between the coastal upwelling direction and the trajectory of the high-pressure system movement is likely a key influencing factor in determining the magnitude of upwelling weakening during AMHW events. Previous studies have indicated that the subtropical high-pressure system in the northwestern Pacific is located around 20°N and develops from southeast to northwest, often traversing the study area [54,69,70]. As mentioned earlier, for an AMHW event to occur near the wind-driven upwelling region, the wind anomalies often point in an unfavorable direction. Therefore, the presence of the anticyclonic high-pressure center triggering the corresponding AMHW event in the E region requires it to be positioned in the northwest of the E region (Figure 8d). Similarly, for an AMHW event in the NE region, with anomalous northwesterly winds prevailing, the high-pressure center needs to appear in the southwest of the NE region (Figure 8e). Thirdly, due to the trajectory of the high-pressure center moving from southeast to northwest through the study area, the high-pressure center triggering AMHW events in the NE region can only appear near Hainan Island, while the high-pressure center inducing AMHW events in the E region is more likely to be located far from Hainan Island and on the northern side of the Beibu Gulf (Figure 8d,e). Consequently, the upwelling in the NE region, which is in closer proximity to the high-pressure center during the AMHW period, experiences lower wind speeds.

Surprisingly, in the W region, the climatological wind direction anomalies of coastal wind vectors during Delta AMHW are favorable for upwelling, but the Chl-*a* does not increase (Figures 8c and 9c). First, the cause may be that during pre-AMHW, the wind vectors are precisely eastward and horizontal to the mouth of the Beibu Gulf, causing a large amount of water to accumulate within the bay (Figure 8i). The nutrients transported by the Western Guangdong coastal current are mostly confined to the northern bay, resulting in widespread phytoplankton blooms along the entire coastal area of western Hainan Island and positive Chl-*a* anomalies within the Beibu Gulf (Figure 9i) [64,71]. During AMHW, however, the wind vector anomalies are southward, perpendicular to the mouth of the Beibu Gulf, and the wind no longer promotes water accumulation. As a result, the Chl-*a* in the W region decreases despite the favorable wind conditions for upwelling. Secondly, as wave mixing enhanced by increased wind speed promotes the intensity of W region upwelling [34], the reduced wind speed during AMHW leads to a weaker upwelling intensity in the W region. This positive correlation between wind and upwelling in the W region is directly illustrated in Figure 6a.

In addition, stratification is an important influencing factor that alters the intensity of upwelling. The depth of the upwelling source is closely related to its strength and decreases with increasing stratification [72,73]. Similarly, the fishery resources in the upwelling ecosystems also decrease with increasing stratification [74]. Strong correlations between the sea surface stratification and Chl-*a* can be observed, reaching −0.84, −0.81, and −0.72 in the E, NE, and W regions, respectively (Figure 5). Additionally, both stratification indices and MHW intensity are closely related to temperature, exhibiting consistent and strong correlations of above 0.85 (Figure 5). This suggests that MHW intensity is essentially a measure of temperature stratification and is also influenced by atmospheric forcing, albeit with a lag compared to the latter.

As previously mentioned, during AMHW, the NE region exhibits the smallest Chl-*a* concentration, indicating the strongest inhibition by AMHW, followed by the W region, and the E region with the lowest inhibition. The higher correlation between upwelling in the NE region and both stratification and wind, along with the greater magnitude of wind stress weakening and stratification enhancement in the NE region, can also explain this phenomenon (Figure 3b,c, Figure 4b,c and Figure 5b). In contrast, despite experiencing the largest reduction in wind stress, the decrease in Chl-*a* concentration in the W region is limited (Figure 4a,c), primarily due to its tidal origin rather than wind-driven processes. Cross-correlation results between stratification intensity and Chl-*a* demonstrate that the variations in Chl-*a* in all three regions lag behind stratification by approximately 1 day (Figure 6d). The minimum values of Chl-*a* occur between +1 and +8 days. The changes in Chl-*a* during AMHW in the three upwelling regions lag behind wind stress by approximately 1–6 days (Figures 4 and 5a,c), which is consistent with the cross-correlation results between Chl-*a* and wind stress and wind stress curl (Figure 6c,d). However, in the NE and W regions, the cross-correlation coefficients between Chl-*a* and wind stress and wind stress curl reach their maximum values at lag days of 0–1, indicating almost no lag effect. Thus, similar to the W region, the NE region may be influenced by the Western Guangdong coastal current [64,71,75].

4.3. The Contributions of Stratification Enhancement and Wind Weakening to the Decrease in Chl-a Concentration during Different Phases of AMHW

Due to the lagged days between Chl-*a* and wind stress during AMHW (4, 0, and 1 for the E, NE, and W regions, respectively), linear regression analyses were performed between the Chl-*a* series lagged by the corresponding days and wind stress and stratification intensity. Strong linear relationships were observed in all three regions (Figure 7). Particularly, after conducting bivariate linear regression, the R^2 values for the linear functions between Chl-*a* and these two factors reached 0.7, 0.68, and 0.58 for the E, NE, and W regions, respectively. The coefficients of the stratification component in the bivariate regression were −0.37, −0.78, and −0.64 for the E, NE, and W regions, respectively, indicating that the NE region is mostly influenced by stratification, followed by the W region, which is slightly less influenced but still significantly more than the E region. The coefficients of the wind stress component in the three regions were 5.3, 3.3, and 1.6, respectively. By combining these

coefficients, it can be concluded that the upwelling in the W region is more susceptible to stratification, while the upwelling in the E region is more influenced by wind stress, and the NE region is sensitive to changes in both processes.

Based on the results of bivariate linear regression, the contributions of wind weakening and stratification strengthening in the three upwelling regions during different periods of AMHW to the reduction in Chl-*a* or upwelling inhibition can be quantified. From the perspective of the total AMHW period, including the pre-AMHW phase, the absolute contributions of wind weakening to the reduction in Chl-*a* concentration are consistent for the E and NE regions. On the other hand, the absolute contribution of stratification strengthening to the reduction in Chl-*a* concentration is approximately 1/5 higher for the NE region compared to the W region and twice as high compared to the E region (Figure 10). In terms of the proportion between the two contributions, the contribution of wind stress in the E region is twice as high as in the NE regions. Thus, wind and stratification in the E and NE regions promote the development of upwelling during the pre-AMHW phase. However, during the development phase, they shift to inhibiting factors, with wind stress still playing a significant role. When AMHW reaches its mature phase, the inhibitory effects of both factors are at their strongest. In the decline phase, stratification mainly plays a role, as the wind field, which was initially favorable for AMHW, has already returned to normal due to the movement and changes in the high-pressure center, leaving only the heated SST to continue inhibiting upwelling.

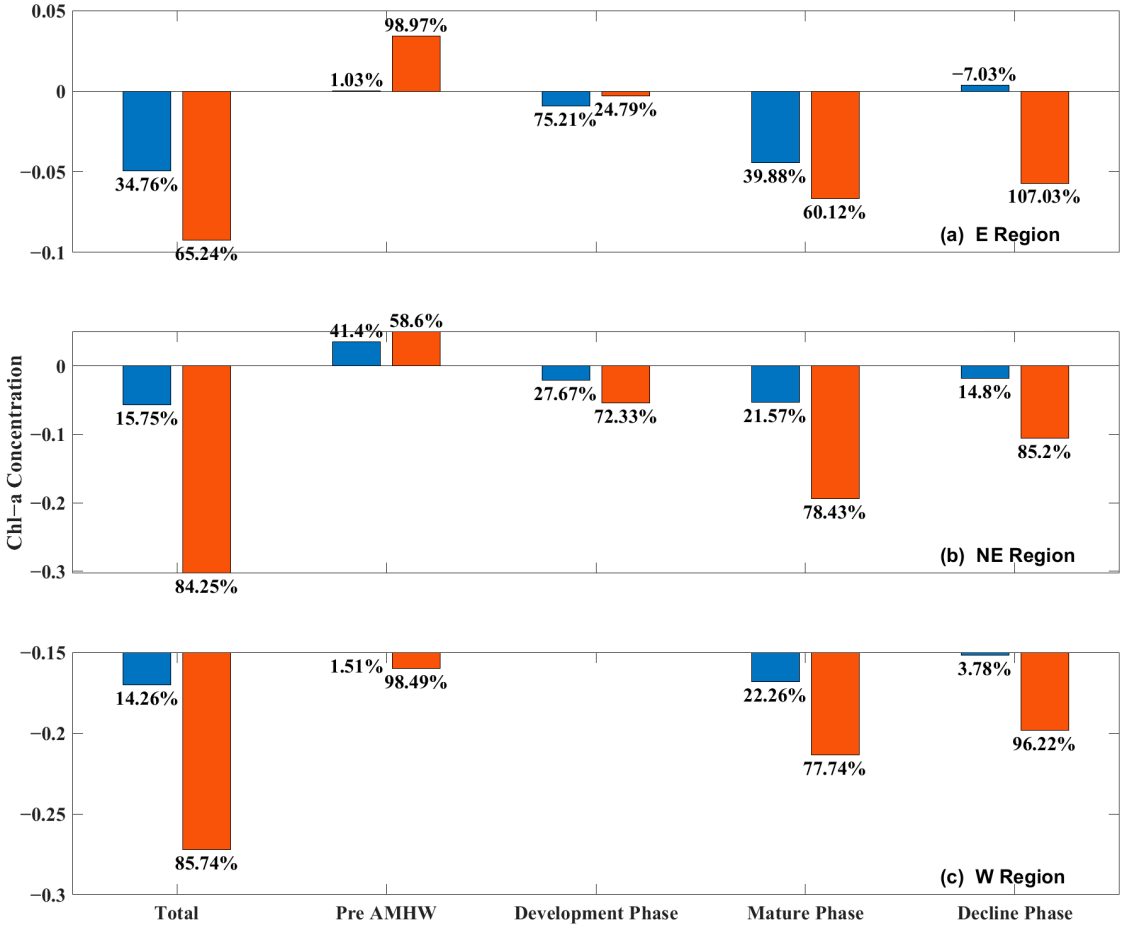

Figure 10. Contributions and Relative Percentages of Wind and Stratification Effects on Chl-*a* Variations in Three Upwelling Regions during Different Phases of AMHW. Blue represents the wind stress component, and red represents the stratification component. There is not a development phase and stress component in the W region; thus, the values are not shown.

4.4. The Impact of AMHW on Marine Ecosystems

During the summer AMHW in the northwestern SCS, three distinct upwelling are inhibited to varying degrees through stratification enhancement and wind weakening (Figure 11), with greater inhibition by the stronger AMHW intensity. Although, in some regions, the pre-mature AMHW wind patterns are favorable for upwelling, the intensification and prolonged duration of heatwaves are expected to further accelerate this trend under global warming [27,76]. This will inevitably lead to a long-term weakening of upwelling, causing a severe impact on ecosystems. Over the past decades, the reduction in oceanic upwelling along the Iberian Peninsula coast has been driving ecosystems towards an irreversible direction, characterized by an increased frequency of harmful algal blooms and decreased sardine catches [77]. As a renowned fishing ground located in the upwelling zone on the eastern side of Hainan Island, the Qinglan fishing ground exerts a significant influence on the growth of phytoplankton and the distribution and abundance of zooplankton [78]. The weakening of upwelling could significantly alter the continental shelf ecosystem in the northwestern SCS [78–80]. The traditional view suggests that upwelling regions serve as refuges for temporary climate change impacts on coral reefs in the face of heatwave disturbances [81,82]. The northwestern Beibu Gulf and the eastern coast of Hainan Island are both rich in coral reef resources [42,83]. However, as offshore upwelling weakens in the future, these coral reefs will face increasingly challenging conditions.

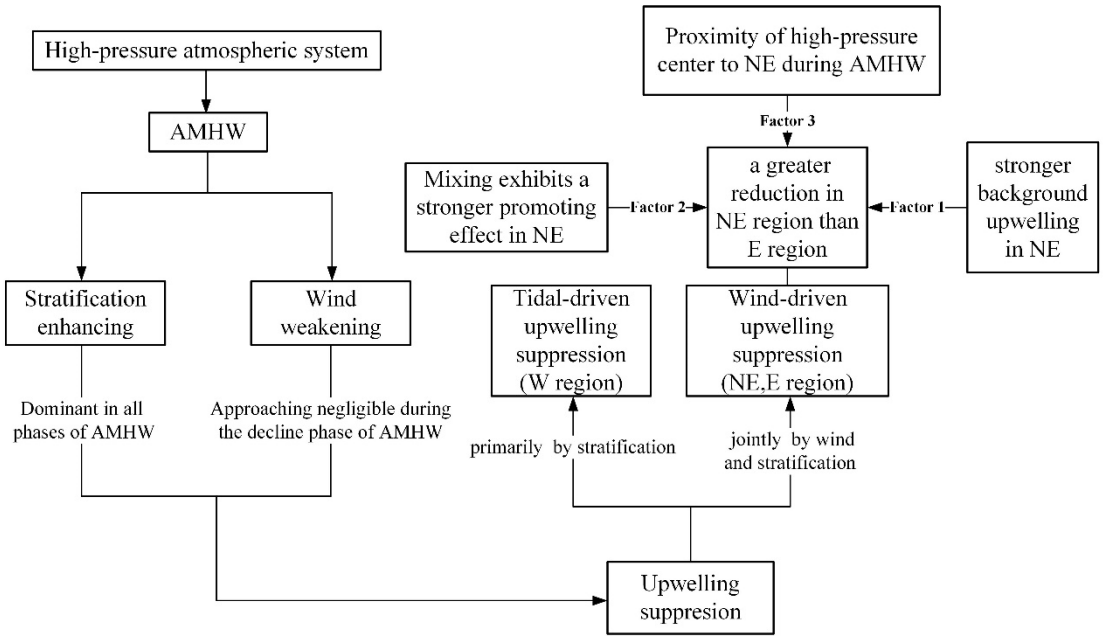

Figure 11. The diagram of AMHW-induced Suppression of Three Distinct Upwelling Systems.

5. Conclusions

Based on satellite remote sensing data, this study analyzes the synthetic sequence of AMHW events (30 days before and after the occurrence of heatwaves) in three different upwelling regions in the northwest SCS from 1998 to 2021. Two prominent features during AMHW, namely, wind stress reduction and stratification intensification, significantly suppressed the intensity of upwelling in those regions. During AMHW, all three upwelling regions were inhibited by enhanced seawater stratification. By contrast, the upwelling in the W region is inhibited by enhanced seawater stratification. The upwelling in both the E and NE regions is wind-driven, regulated by both wind and stratification simultaneously. However, due to the combined influence of multiple factors, the NE region experiences a greater reduction in upwelling compared to the E region. The causes could be the following: (1) the background upwelling in the NE region is stronger than in the E; (2) Mixing triggered by wind exhibits a stronger promoting effect; (3) The coastline of the upwelling region,

in conjunction with the movement trajectory of the high-pressure system, determines the location of the high-pressure center during the occurrence of AMHW. Specifically, during the NE region's AMHW period, the high-pressure center is positioned in closer proximity to the upwelling area. To quantify the contributions of wind stress and stratification changes during AMHW to the variations in upwelling, linear fits were performed between Chl-*a* and wind stress and stratification intensity. It was found that during the total period in all regions, stratification had an overwhelmingly dominant inhibitory effect on Chl-*a*, but the contribution of wind stress was much stronger in the E region. During the pre-AMHW period, both wind and stratification factors positively promote wind-driven upwelling in the E and NE regions. However, as AMHW develops, the promoting effect transitions into an inhibiting effect. The three upwelling regions experience the maximum inhibition during the mature phase. After entering the decline phase, the influence of wind stress becomes negligible, and the inhibition of Chl-*a* concentration is primarily attributed to stratification effects.

Author Contributions: Conceptualization, S.L., Q.L. and F.C.; Methodology, S.L.; Software, S.L.; Validation, F.C.; Formal analysis, S.L. and Q.L.; Resources, F.C.; Data curation, S.L.; Writing—original draft, S.L. and Q.L.; Writing—review & editing, S.L., Q.L., X.Z., G.J., C.C. and F.C.; Visualization, S.L.; Supervision, F.C.; Project administration, F.C.; Funding acquisition, F.C. All authors have read and agreed to the published version of the manuscript.

Funding: This study was supported by the National Natural Science Foundation of China (U1901213, 92158201, 42276047), Entrepreneurship Project of Shantou (2021112176541391), Scientific Research Start-Up Foundation of Shantou University (NTF20006), and Guangdong Provincial College Innovation Team Project (2019KCXTF021).

Data Availability Statement: Data are contained within the article.

Conflicts of Interest: The authors declare no conflict of interest.

References

1. Hu, J.; Wang, X.H. Progress on upwelling studies in the China seas. *Rev. Geophys.* **2016**, *54*, 653–673. [CrossRef]
2. Bakun, A. Global climate change and intensification of coastal ocean upwelling. *Science* **1990**, *247*, 198–201. [CrossRef] [PubMed]
3. Hu, D. Upwelling and sedimentation dynamics. I. The role of upwelling in sedimentation in the Huanghai Sea and East China Sea—A description of general features. *Chin. J. Oceanol. Limnol.* **1984**, *2*, 12–19.
4. Chavez, F.P. Physical estimates of global new production:the upwelling contribution. In *Upwelling in the Ocean: Modern Processes and Ancient Records*; Wiley; John & Sons: New York, NY, USA, 1995.
5. Pauly, D.; Christensen, V. Primary production required to sustain global fisheries. *Nature* **1995**, *374*, 255–257. [CrossRef]
6. Ianson, D.; Feely, R.A.; Sabine, C.L.; Juranek, L.W. Features of Coastal Upwelling Regions that Determine Net Air-Sea CO_2 Flux. *J. Oceanogr.* **2009**, *65*, 677–687. [CrossRef]
7. Barth, J.A.; Menge, B.A.; Lubchenco, J.; Chan, F.; Bane, J.M.; Kirincich, A.R.; McManus, M.A.; Nielsen, K.J.; Pierce, S.D.; Washburn, L. Delayed upwelling alters nearshore coastal ocean ecosystems in the northern California current. *Proc. Natl. Acad. Sci. USA* **2007**, *104*, 3719–3724. [CrossRef]
8. Xie, S.P.; Xie, Q.; Wang, D.X.; Liu, W.T. Summer upwelling in the South China Sea and its role in regional climate variations. *J. Geophys. Res. Ocean.* **2003**, 108. [CrossRef]
9. Benthuysen, J.A.; Oliver, E.C.J.; Chen, K.; Wernberg, T. Advances in understanding marine heatwaves and their impacts. *Front. Mar. Sci.* **2020**, *7*, 147. [CrossRef]
10. Hughes, T.P.; Anderson, K.D.; Connolly, S.R.; Heron, S.F.; Kerry, J.T.; Lough, J.M.; Baird, A.H.; Baum, J.K.; Berumen, M.L.; Bridge, T.C.; et al. Spatial and temporal patterns of mass bleaching of corals in the Anthropocene. *Science* **2018**, *359*, 80–83. [CrossRef]
11. Smale, D.A.; Wernberg, T.; Oliver, E.C.J.; Thomsen, M.; Harvey, B.P.; Straub, S.C.; Burrows, M.T.; Alexander, L.V.; Benthuysen, J.A.; Donat, M.G.; et al. Marine heatwaves threaten global biodiversity and the provision of ecosystem services. *Nat. Clim. Chang.* **2019**, *9*, 306–312. [CrossRef]
12. Sen Gupta, A.; Thomsen, M.; Benthuysen, J.A.; Hobday, A.J.; Oliver, E.; Alexander, L.V.; Burrows, M.T.; Donat, M.G.; Feng, M.; Holbrook, N.J.; et al. Drivers and impacts of the most extreme marine heatwave events. *Sci. Rep.* **2020**, *10*, 19359. [CrossRef] [PubMed]
13. Seabra, R.; Varela, R.; Santos, A.M.; Gómez-Gesteira, M.; Meneghesso, C.; Wethey, D.S.; Lima, F.P. Reduced nearshore warming associated with eastern boundary upwelling systems. *Front. Mar. Sci.* **2019**, *6*, 104. [CrossRef]
14. Varela, R.; Rodríguez-Díaz, L.; de Castro, M.; Gómez-Gesteira, M. Influence of Eastern Upwelling systems on marine heatwaves occurrence. *Glob. Planet. Chang.* **2021**, *196*, 103379. [CrossRef]

15. García-Reyes, M.; Sydeman, W.J.; Schoeman, D.S.; Rykaczewski, R.R.; Black, B.A.; Smit, A.J.; Bograd, S.J. Under pressure: Climate change, upwelling, and eastern boundary upwelling ecosystems. *Front. Mar. Sci.* **2015**, *2*, 109. [CrossRef]
16. Gruber, N. Warming up, turning sour, losing breath: Ocean biogeochemistry under global change. *Philos. Trans. R. Soc. A-Math. Phys. Eng. Sci.* **2011**, *369*, 1980–1996. [CrossRef] [PubMed]
17. Sousa, M.C.; Ribeiro, A.; Des, M.; Gomez-Gesteira, M.; deCastro, M.; Dias, J.M. NW Iberian Peninsula coastal upwelling future weakening: Competition between wind intensification and surface heating. *Sci. Total Environ.* **2020**, *703*, 134808. [CrossRef] [PubMed]
18. Noh, K.M.; Lim, H.-G.; Kug, J.-S. Global chlorophyll responses to marine heatwaves in satellite ocean color. *Environ. Res. Lett.* **2022**, *17*, 064034. [CrossRef]
19. Tan, H.J.; Cai, R.S.; Wu, R.G. Summer marine heatwaves in the South China Sea: Trend, variability and possible causes. *Adv. Clim. Chang. Res.* **2022**, *13*, 323–332. [CrossRef]
20. Li, Y.; Ren, G.; Wang, Q.; Mu, L.; Niu, Q. Marine Heatwaves in the South China Sea: Tempo-Spatial Pattern and Its Association with Large-Scale Circulation. *Remote Sens.* **2022**, *14*, 5829. [CrossRef]
21. He, W.; Zeng, X.; Deng, L.; Pi, Q.L.C.; Zhao, J. Enhanced impact of prolonged MHWs on satellite-observed chlorophyll in the South China Sea. *Prog. Oceanogr.* **2023**, *218*, 103123. [CrossRef]
22. Li, L. Summer upwelling system over the northern continental shelf of the South China Sea: A physical description. In Proceedings of the Symposium on the Physical and Chemical Oceanography of the China Seas; China Ocean Press: Beijing, China, 1993; pp. 58–68.
23. Lin, P.; Hu, J.; Zheng, Q.; Sun, Z.; Zhu, J. Observation of summertime upwelling off the eastern and northeastern coasts of Hainan Island, China. *Ocean Dyn.* **2016**, *66*, 387–399. [CrossRef]
24. Zhu, J.; Zhou, Q.; Zhou, Q.; Geng, X.; Shi, J.; Guo, X.; Yu, Y.; Yang, Z.; Fan, R. Interannual variation of coastal upwelling around Hainan Island. *Front. Mar. Sci.* **2023**, *10*, 1054669. [CrossRef]
25. Xie, L.; Zhang, S.; Zhao, H. Overview of studies on Qiongdong upwelling. *J. Trop. Oceanogr.* **2012**, *31*, 35–41. (In Chinese)
26. Jing, Z.Y.; Qi, Y.Q.; Hua, Z.L.; Zhang, H. Numerical study on the summer upwelling system in the northern continental shelf of the South China Sea. *Cont. Shelf Res.* **2009**, *29*, 467–478. [CrossRef]
27. Xie, L.; Zong, X.; Yi, X.; Li, M. The interannual variation and long-term trend of Qiongdong upwelling. *Oceanol. Limnol. Sin* **2016**, *47*, 43–51. (In Chinese)
28. Shu, Y.; Wang, Q.; Zu, T. Progress on shelf and slope circulation in the northern South China Sea. *Sci. China Earth Sci.* **2018**, *61*, 560–571. [CrossRef]
29. Song, X.; Lai, Z.; Ji, R.; Chen, C.; Zhang, J.; Huang, L.; Yin, J.; Wang, Y.; Lian, S.; Zhu, X. Summertime primary production in northwest South China Sea: Interaction of coastal eddy, upwelling and biological processes. *Cont. Shelf Res.* **2012**, *48*, 110–121. [CrossRef]
30. Wang, D.; Shu, Y.; Xue, H.; Hu, J.; Chen, J.; Zhuang, W.; Zu, T.; Xu, J. Relative contributions of local wind and topography to the coastal upwelling intensity in the northern South China Sea. *J. Geophys. Res. Ocean.* **2014**, *119*, 2550–2567. [CrossRef]
31. Chen, Z.; Qiao, F.; Xia, C.; Wang, G. The numerical investigation of seasonal variation of the cold water mass in the Beibu Gulf and its mechanisms. *Acta Oceanol. Sin.* **2015**, *34*, 44–54. [CrossRef]
32. Gao, J.; Wu, G.; Ya, H. Review of the circulation in the Beibu Gulf, South China Sea. *Cont. Shelf Res.* **2017**, *138*, 106–119. [CrossRef]
33. Bai, P.; Ling, Z.; Zhang, S.; Xie, L.; Yang, J. Fast-changing upwelling off the west coast of Hainan Island. *Ocean Model.* **2020**, *148*, 101589. [CrossRef]
34. Bai, P.; Yang, J.; Zhang, S.; Xie, L.; Wu, J. Upwelling off the west coast of Hainan Island: Sensitivity to wave-mixing. *Acta Oceanol. Sin.* **2019**, *38*, 11–19. [CrossRef]
35. Lue, X.; Qiao, F.; Wang, G.; Xia, C.; Yuan, Y. Upwelling off the west coast of Hainan Island in summer: Its detection and mechanisms. *Geophys. Res. Lett.* **2008**, 35. [CrossRef]
36. Hobday, A.J.; Alexander, L.V.; Perkins, S.E.; Smale, D.A.; Straub, S.C.; Oliver, E.C.J.; Benthuysen, J.A.; Burrows, M.T.; Donat, M.G.; Peng, M.; et al. A hierarchical approach to defining marine heatwaves. *Prog. Oceanogr.* **2016**, *141*, 227–238. [CrossRef]
37. Good, S.; Fiedler, E.; Mao, C.; Martin, M.J.; Maycock, A.; Reid, R.; Roberts-Jones, J.; Searle, T.; Waters, J.; While, J.; et al. The current configuration of the OSTIA system for operational production of foundation sea surface temperature and ice concentration analyses. *Remote Sens.* **2020**, *12*, 720. [CrossRef]
38. Hersbach, H.; Bell, B.; Berrisford, P.; Biavati, G.; Horányi, A.; Muñoz Sabater, J.; Nicolas, J.; Peubey, C.; Radu, R.; Rozum, I. ERA5 monthly averaged data on single levels from 1979 to present. *Copernic. Clim. Chang. Serv. Clim. Data Store* **2019**, *10*, 252–266.
39. Price, J.F. Upper Ocean response to a hurricane. *J. Phys. Oceanogr.* **1981**, *11*, 153–175. [CrossRef]
40. Yelland, M.J.; Moat, B.I.; Taylor, P.K.; Pascal, R.W.; Hutchings, J.; Cornell, V.C. Wind stress measurements from the open ocean corrected for airflow distortion by the ship. *J. Phys. Oceanography.* **1998**, *28*, 1511–1526. [CrossRef]
41. Schlegel, R.W.; Smit, A.J. heatwaveR: A central algorithm for the detection of heatwaves and cold-spells. *J. Open Source Softw.* **2018**, *3*, 821. [CrossRef]
42. Zhao, Z.; Marin, M. A MATLAB toolbox to detect and analyze marine heatwaves. *J. Open Source Softw.* **2019**, *4*, 1124. [CrossRef]
43. Zhan, W.; Zhang, Y.; He, Q.; Zhan, H. Shifting responses of phytoplankton to atmospheric and oceanic forcing in a prolonged marine heatwave. *Limnol. Oceanogr.* **2023**, *68*, 1821–1834. [CrossRef]

44. Dalsin, M.; Walter, R.K.; Mazzini, P.L.F. Effects of basin-scale climate modes and upwelling on nearshore marine heatwaves and cold spells in the California Current. *Sci. Rep.* **2023**, *13*, 12389. [CrossRef] [PubMed]
45. Jung, J.; Cho, Y.-K. Effects of Surface Heating on Coastal Upwelling Intensity. *J. Geophys. Res. Ocean.* **2023**, *128*, e2022JC018795. [CrossRef]
46. Bond, N.A.; Cronin, M.F.; Freeland, H.; Mantua, N. Causes and impacts of the 2014 warm anomaly in the NE Pacific. *Geophys. Res. Lett.* **2015**, *42*, 3414–3420. [CrossRef]
47. Rodrigues, R.R.; Taschetto, A.S.; Sen Gupta, A.; Foltz, G.R. Common cause for severe droughts in South America and marine heatwaves in the South Atlantic. *Nat. Geosci.* **2019**, *12*, 620–626. [CrossRef]
48. Yao, Y.; Wang, C. Variations in summer marine heatwaves in the South China Sea. *J. Geophys. Res. Ocean.* **2021**, *126*, e2021JC017792. [CrossRef]
49. He, C.; Zhou, T.; Lin, A.; Wu, B.; Gu, D.; Li, C.; Zheng, B. Enhanced or weakened western North Pacific subtropical high under global warming? *Sci. Rep.* **2015**, *5*, 16771. [CrossRef] [PubMed]
50. Kosaka, Y.; Xie, S.-P.; Lau, N.-C.; Vecchi, G.A. Origin of seasonal predictability for summer climate over the Northwestern Pacific. *Proc. Natl. Acad. Sci. USA* **2013**, *110*, 7574–7579. [CrossRef]
51. Wang, B.; Wu, R.; Lau, W. Interannual Variability of the Asian Summer Monsoon: Contrasts between the Indian and the Western North Pacific-East Asian Monsoons. *J. Clim.* **2001**, *14*, 4073–4090. [CrossRef]
52. Wang, B.; Xiang, B.; Lee, J.-Y. Subtropical High predictability establishes a promising way for monsoon and tropical storm predictions. *Proc. Natl. Acad. Sci. USA* **2013**, *110*, 2718–2722. [CrossRef]
53. Wu, B.; Zhou, T.; Li, T. Seasonally Evolving Dominant Interannual Variability Modes of East Asian Climate. *J. Clim.* **2009**, *22*, 2992–3005. [CrossRef]
54. Feng, Y.; Bethel, B.J.; Dong, C.; Zhao, H.; Yao, Y.; Yu, Y. Marine heatwave events near Weizhou Island, Beibu Gulf in 2020 and their possible relations to coral bleaching. *Sci. Total Environ.* **2022**, *823*, 153414. [CrossRef] [PubMed]
55. Yoon, D.; Cha, D.-H.; Lee, G.; Park, C.; Lee, M.-I.; Min, K.-H. Impacts of Synoptic and Local Factors on Heat Wave Events over Southeastern Region of Korea in 2015. *J. Geophys. Res.-Atmos.* **2018**, *123*, 12081–12096. [CrossRef]
56. Sohn, B.-J.; Chung, H.-S.; Kim, D.; Perkey, D.; Robertson, F.; Smith, E. Use of Satellite-Derived Water Vapor Data to Investigate Northwestward Expansion of North Pacific Subtropical High during 1995 Summer. *J. Meteorol. Soc. Jpn.* **2001**, *79*, 1059–1075. [CrossRef]
57. Benazzouz, A.; Pelegrí, J.L.; Demarcq, H.; Machín, F.; Mason, E.; Orbi, A.; Peña-Izquierdo, J.; Soumia, M. On the temporal memory of coastal upwelling off NW Africa. *J. Geophys. Res. Ocean.* **2014**, *119*, 6356–6380. [CrossRef]
58. Marcello, J.; Hernández-Guerra, A.; Eugenio, F.; Fonte, A. Seasonal and temporal study northwest African upwelling System. *Int. J. Remote Sens.* **2011**, *32*, 1843–1859. [CrossRef]
59. Shi, W.; Huang, Z.; Hu, J. Using TPI to Map Spatial and Temporal Variations of Significant Coastal Upwelling in the Northern South China Sea. *Remote Sens.* **2021**, *13*, 1065. [CrossRef]
60. Shu, Y.; Wang, D.; Feng, M.; Geng, B.; Chen, J.; Yao, J.; Xie, Q.; Liu, Q.Y. The contribution of local wind and ocean circulation to the interannual variability in coastal upwelling intensity in the Northern South China Sea. *J. Geophys. Res. Ocean.* **2018**, *123*, 6766–6778. [CrossRef]
61. Jung, J.; Cho, Y.-K. Persistence of coastal upwelling after a plunge in upwelling-favourable wind. *Sci. Rep.* **2020**, *10*, 11938. [CrossRef]
62. Bakun, A. *Coastal Upwelling Indices, West Coast of North America, 1946-71*; NOAA Technical Report NMFS SSRF; National Marine Fisheries Service: Silver Spring, MD, USA, 1973; Volume 671.
63. Bakun, A. *Daily and Weekly Upwelling Indices, West Coast of North America, 1967-73*; NOAA Technical Report NMFS SSRF; National Marine Fisheries Service: Silver Spring, MD, USA, 1975; Volume 693.
64. Lao, Q.; Lu, X.; Chen, F.; Jin, G.; Chen, C.; Zhou, X.; Zhu, Q. Effects of upwelling and runoff on water mass mixing and nutrient supply induced by typhoons: Insight from dual water isotopes tracing. *Limnol. Oceanogr.* **2023**, *68*, 284–295. [CrossRef]
65. Kunarso, K.; Hadi, S.; Ningsih, N.; Baskoro, M.; Wirasatriya, A.; Kuswardani, A. The classification of upwelling indicators base on sea surface temperature, chlorophyll-a and upwelling index, the case study in Southern Java to Timor Waters. *IOP Conf. Ser. Earth Environ. Sci.* **2020**, *530*, 012020. [CrossRef]
66. Shang, S.; Zhang, C.; Hong, H.; Shang, S.P.; Chai, F. Short-term variability of chlorophyll associated with upwelling events in the Taiwan Strait during the southwest monsoon of 1998. *Deep Sea Res. Part II Top. Stud. Oceanogr.* **2004**, *51*, 1113–1127. [CrossRef]
67. Su, J.; Pohlmann, T. Wind and topography influence on an upwelling system at the eastern Hainan coast. *J. Geophys. Res. Ocean.* **2009**, *114*, C06017. [CrossRef]
68. Bai, P.; Gu, Y.; Li, P.; Wu, K. Modelling the upwelling offthe east Hainan Island coast in summer 2010. *Chin. J. Oceanol. Limnol.* **2016**, *34*, 1358–1373. [CrossRef]
69. Choi, W.; Kim, K.-Y. Summertime variability of the western North Pacific subtropical high and its synoptic influences on the East Asian weather. *Sci. Rep.* **2019**, *9*, 7865. [CrossRef] [PubMed]
70. Huang, Q.; Yin, X.; Yao, S. The Quasi-Biweekly Oscillation of Summer Rainfall in Southern China and Its Relationship with the Geopotential Height Anomaly over the North Atlantic Ocean. *Front. Earth Sci.* **2021**, *9*, 770253. [CrossRef]
71. Lao, Q.; Liu, S.; Ling, Z.; Jin, G.; Chen, F.; Chen, C.; Zhu, Q. External Dynamic Mechanisms Controlling the Periodic Offshore Blooms in Beibu Gulf. *J. Geophys. Res. Ocean.* **2023**, *128*, e2023JC019689. [CrossRef]

72. Jacox, M.G.; Edwards, C.A. Effects of stratification and shelf slope on nutrient supply in coastal upwelling regions. *J. Geophys. Res. Ocean.* **2011**, *116*, C03019. [CrossRef]
73. Lentz, S.J.; Chapman, D.C. The importance of nonlinear cross-shelf momentum flux during wind-driven coastal upwelling. *J. Phys. Oceanogr.* **2004**, *34*, 2444–2457. [CrossRef]
74. Narvekar, J.; Roy Chowdhury, R.; Gaonkar, D.; Kumar, P.; Kumar, S.P. Observational evidence of stratification control of upwelling and pelagic fishery in the eastern Arabian Sea. *Sci. Rep.* **2021**, *11*, 7293. [CrossRef]
75. Lao, Q.; Zhang, S.; Li, Z.; Chen, F.; Zhou, X.; Jin, G.; Huang, P.; Deng, Z.; Chen, C.; Zhu, Q. Quantification of the seasonal intrusion of water masses and their impact on nutrients in the Beibu Gulf using dual water isotopes. *J. Geophys. Res. Ocean.* **2022**, *127*, e2021JC018065. [CrossRef]
76. Su, J.; Xu, M.; Pohlmann, T.; Xu, D.; Wang, D. A western boundary upwelling system response to recent climate variation (1960–2006). *Cont. Shelf Res.* **2013**, *57*, 3–9. [CrossRef]
77. Perez, F.F.; Padin, X.A.; Pazos, Y.; Gilcoto, M.; Cabanas, M.; Pardo, P.C.; Dolores Doval, M.; Farina-Busto, L. Plankton response to weakening of the Iberian coastal upwelling. *Glob. Chang. Biol.* **2010**, *16*, 1258–1267. [CrossRef]
78. Li, K.; Yin, J.; Huang, L.; Zhang, J.; Lian, S.; Liu, C. Distribution and abundance of thaliaceans in the northwest continental shelf of South China Sea, with response to environmental factors driven by monsoon. *Cont. Shelf Res.* **2011**, *31*, 979–989. [CrossRef]
79. Li, K.Z.; Yin, J.Q.; Huang, L.M.; Lian, S.M.; Zhang, J.L.; Liu, C.G. Monsoon-forced distribution and assemblages of appendicularians in the northwestern coastal waters of South China Sea. *Estuar. Coast. Shelf Sci.* **2010**, *89*, 145–153. [CrossRef]
80. Yin, J.; Huang, L.; Li, K.; Lian, S.; Li, C.; Lin, Q. Abundance distribution and seasonal variations of *Calanus sinicus* (Copepoda: Calanoida) in the northwest continental shelf of South China Sea. *Cont. Shelf Res.* **2011**, *31*, 1447–1456. [CrossRef]
81. Randall, C.J.; Toth, L.T.; Leichter, J.J.; Maté, J.L.; Aronson, R.B. Upwelling buffers climate change impacts on coral reefs of the eastern tropical Pacific. *Ecology* **2020**, *101*, e02918. [CrossRef]
82. West, J.M.; Salm, R.V. Resistance and resilience to coral bleaching: Implications for coral reef conservation and management. *Conserv. Biol.* **2003**, *17*, 956–967. [CrossRef]
83. Liu, B.; Guan, L.; Chen, H. Detecting 2020 coral bleaching event in the Northwest Hainan Island using CORALTEMP SST and sentinel-2b MSI imagery. *Remote Sens.* **2021**, *13*, 4948. [CrossRef]